JMEPEG (2004) 13:493-503
DOI: 10.1361/10599490419234
©ASM International
1059-9495/$19.00

Creep Deformation Behavior and Failure Diagnostic Diagrams of a Columnar-Grained Nickel-Based Superalloy

Gopalakrishna Magadi and V.M. Radhakrishnan

(Submitted January 2, 2003)

Uniaxial creep deformation of a columnar-grained cast Ni-based superalloy has been analyzed in the temperature range of 1035-1315 K. Two-stage heat treatment of the material resulted in an average γ' particle size of 0.4 μm and inter-particle distance of 0.04 μm. At 1035 K, the alloy showed predominantly primary creep with very low tertiary creep strains. At temperatures above 1035 K, a pseudo-tertiary creep regimen is predominant. Faceted fracture, coarsening of γ' particles, decohesion of the matrix around the particles, and rafting of the coarsened γ' particles have been observed as failure modes over the temperature range studied. An analysis is presented to understand creep deformation behavior of the material in the secondary and tertiary creep stages, by expressing them as power functions of time. Failure diagnostic diagrams have also been constructed for the material over the temperature range investigated.

Keywords creep, creep rate, directional solidification, failure diagnostic diagram, fracture, Ni-based superalloy, rupture time

1. Introduction

The strength of cast nickel-base superalloys is derived from the precipitation of a high volume fraction of gamma prime (γ') cuboids in the gamma (γ) matrix. Directionally solidified (DS) superalloys exhibit higher creep strength than conventionally cast alloys with an equiaxed grain microstructure. With proper thermal gradient and solidification rate, DS alloys can be grown with large elongated columnar grains. Finer and more uniformly precipitated γ' particles can be achieved by proper solution and aging treatments. The secondary creep rate of DS superalloys is usually much lower than that of equiaxed superalloys.[1] In DS alloys, the transverse grain boundary is minimized and the tertiary creep behavior is quite extensive due to reduced grain boundary failure initiation sites.[2] The rupture time increases as the mean grain aspect ratio (defined as the ratio of mean grain length to mean grain width) increases. Crystallograhic orientation of grains also affects the creep behavior of DS superalloys where a large angular deviation between the loading-axis and the crystallographic orientation of the grains reduces the creep strength, causing the DS superalloy to almost behave like a conventionally cast equiaxed alloy.[3-5]

Gopalakrishna Magadi, American Bureau of Shipping, 165855 Northchase Drive, Houston, TX 77060. **V.M. Radhakrishnan,** formerly Emeritus Professor, Indian Institute of Technology, Madras 600036, India. Contact e-mail: gmagadi@eagle.org.

Disclaimer: The views expressed in this paper are solely those of the authors alone and do not reflect in any way those of the American Bureau of Shipping.

The DS cast nickel-base superalloy investigated is a candidate material for turbine blades in gas-turbine engines. The present investigation has been undertaken to study the creep behavior of DS CM 247LC alloy, which is an improved version of MAR-M 247, with about 65 vol.% γ' precipitates.

2. Experimental Procedures

The nominal chemical composition of the alloy in weight percent is 8.3 Cr, 9.3 Co, 9.5 W, 3.2 Ta, 5.5 Al, 0.75 Ti, 1.5 Hf, 0.5 Mo, 0.015 Zr, 0.075 C, 0.015 B, and the balance Ni. The alloy was obtained as remelted bar stocks (test certified) from the alloy manufacturer. The DS alloy was produced in the laboratory using these bar stocks. The alloy was melted in an industrial vacuum DS furnace using a stabilized zirconia crucible. The melt was poured at 1873 K through a tundish with a ceramic filter into the ceramic shell mould maintained at 1773 K and mounted on a water-cooled copper chill plate. The shell was withdrawn at a rate of 30 cm/h. The entire operation was carried out under vacuum (less than 10 μm Hg).

The heat treatment schedule given to the alloy is as follows: (a) Solution treatment under vacuum (10^{-4} torr) 1503 K for 2 h + 1553 K for 2 h with a ramp rate of 1 K/min + Ar gas fan quenching (ArGFQ); (b) first stage ageing treatment in vacuum 1353 K for 4 h + ArGFQ; and (c) second stage aging treatment in vacuum 1143 K for 20 h + forced air-cooling.

Typical optical and transmission electron microscope (TEM) images of the alloy are shown in Fig. 1(a-e). The microstructure consists of fine carbides with dendritic sub-structure within the columnar grains (Fig. 1a, 1b, and 1c). An average primary and secondary dendrite arm spacing of 250 and 45 μm are, respectively, observed for the rod samples. A γ-γ' eutectic phase has also been identified (Fig. 1d). Submicron size γ' particles are also observed (Fig. 1e, TEM micrograph). Upon solution treatment the secondary γ' is found to be almost completely absent. Cuboidal γ' and its bimodal distribution have been observed in the aged condi-

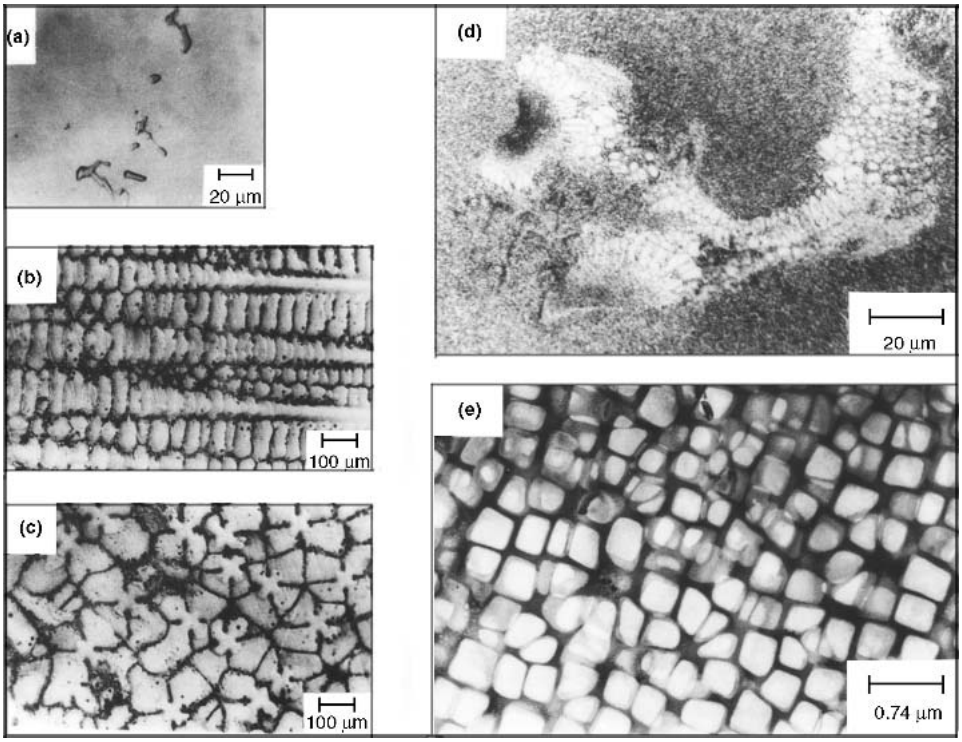

Fig. 1 Optical and TEM micrographs of the alloy: **(a)** carbides, **(b)** longitudinal, and **(c)** transverse sections of dendritic structure in columnar grains, **(d)** γ-γ' eutectic phase, and **(e)** submicron-sized γ' particles

tions of the alloy. The bimodal distribution of γ' results in an optimum combination of tensile [ultimate tensile strength (UTS): 1090 MPa; yield stress (YS): 1010 MPa; 10% elongation (EL)] and creep properties for the alloy. The average size of the γ' particles is 0.4 μm with an interparticle distance of around 0.04 μm. The volume percentage of γ' is around 65%.

Round specimens having a gauge length (GL = 5d, where d is the gage diameter) of 25 mm were used for the creep studies. Grain width ranged from 0.5 to 5.0 mm, and the grain aspect ratio was about 8 for a 5 mm grain. Texture studies indicated that a deviation from the vertical of 10-15° in orientation existed in all tensile and creep specimens. The grain boundaries were parallel to the loading axis in the alloy so that grain boundary sliding was highly unlikely. Thus, in the present investigation the alloy did not show any ductility minimum. Typical variations of strength and ductility in the alloy over the temperature range are shown in Fig. 2.

Creep experiments were carried out at specimen temperatures of 1035, 1145, 1255, and 1315 K. The temperature was measured and controlled within ±2 K using a Pt/Pt-13% Rh thermocouple. The specimen elongation was continuously monitored and recorded using a linear variable displacement transducer (LVDT) with a displacement accuracy of ±2 μm. The stress level ranged from 80 to 850 MPa in the investigation.

Optical, transmission electron microscope (TEM), and scanning electron microscope (SEM) fractographic investigations were carried out on crept samples to document the fracture mode, particle coarsening, and crack initiation sites. The details of the experimental procedures are given elsewhere.[6,7]

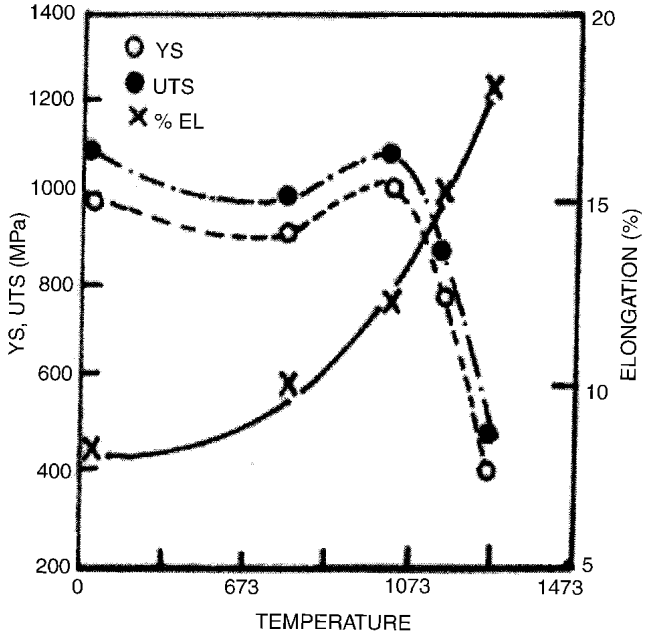

Fig. 2 Variation of ultimate strength, yield strength and elongation with temperature

3. Results and Discussion

3.1 Analysis of Creep Deformation

Figure 3 shows the typical creep deformation with time under different stress levels at 1255 K. There is no primary

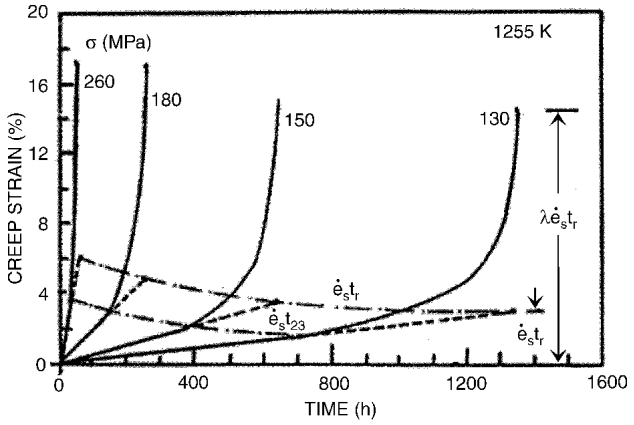

Fig. 3 Typical creep curve at 1255 K

creep. Initially the creep rate is constant; however, it increases during tertiary creep and occupies a large percentage of the total creep strain. Such a tendency has been observed in the temperature range of 1145-1315 K. At 1035 K, primary creep was observed at all stress levels. The contours of the quantities $\dot{e}_s t_r$ and $\dot{e}_s t_{23}$ are also indicated in the figure where $\dot{e}_s$ is defined as the minimum creep rate, t_r is the rupture time, and t_{23} is the time from the beginning of the secondary stage to the beginning of tertiary stage. The creep rupture strain (e_r) is given by $[\lambda \dot{e}_s t_r]$ where λ is the creep ductility index.

Figure 4 shows the modified Monkman–Grant relation given in the form:

$$\frac{\dot{e}_s t_r}{e_r} = \frac{1}{\lambda} \qquad \text{(Eq 1)}$$

Large scatter has been observed in the experimental data indicating the limitation of the above relation as applied to the present material. With $[f = t_{23}/t_r]$ the relation between λ and *1/f* is shown in Fig. 5. The values of *1/f* lie in the range of 1.25-1.9 for the temperature range used in the present investigation. However, the creep ductility index λ varies over a wide range. At higher temperatures, it increases to a level between 6 and 9.

Figure 6 shows the relation between t_{23} and t_r, on a log-log plot. The experimental results indicate a relation of the type:

$$t_{23} = \mathrm{C}\,(t_r)^{0.9} \qquad \text{(Eq 2)}$$

where C is a constant equal to unity in the present case.

Evans and Wilshire[8] have indicated that the tertiary creep strain e_3 can be expressed as a function of time in the form:

$$e_3 = \theta_3\,[\exp(\theta_4 t) - 1] \qquad \text{(Eq 3)}$$

where θ_3 and θ_4 are temperature and stress dependent constants. As an alternative, the different stages of creep can be described by simple power functions of time, and thus, the secondary and tertiary stages of creep can be described through the following relations[9]:

$$e_2 = B_2\, t \quad \text{and} \quad e_3 = B_3\, t^{X3} \qquad \text{(Eq 4)}$$

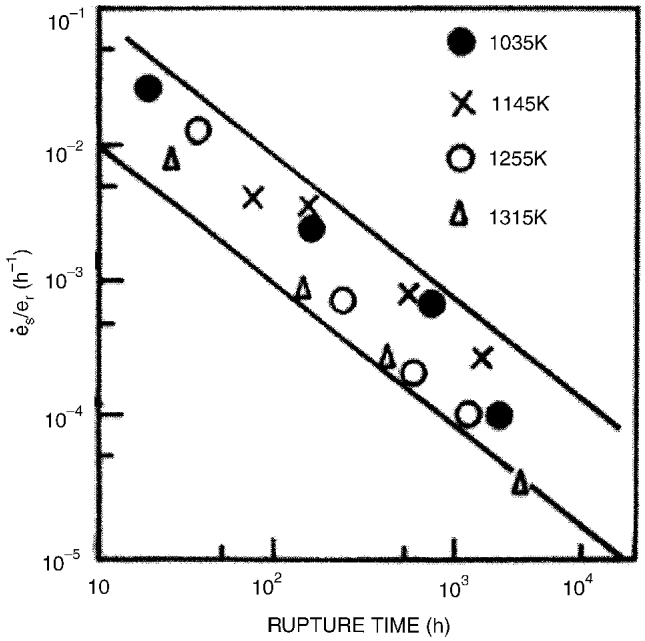

Fig. 4 Relation between ($\dot{e}_s/e_r$) versus rupture time (t_r)

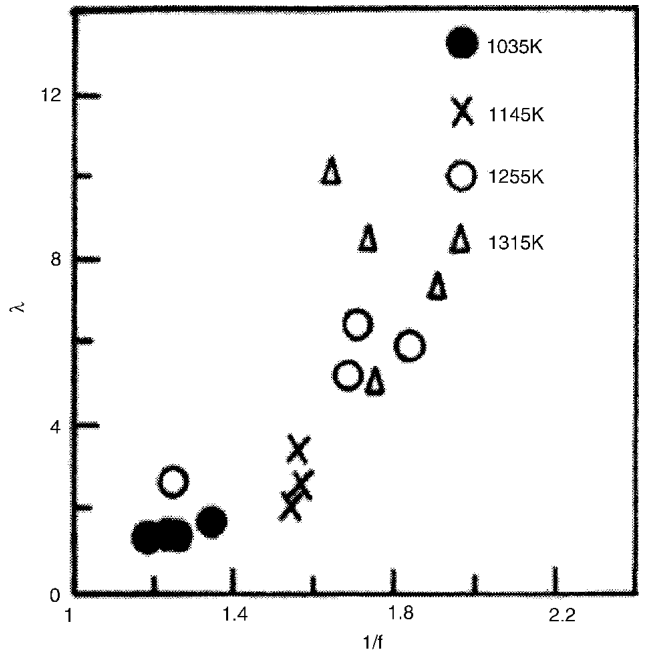

Fig. 5 Relation between creep ductility index (λ) and *1/f*

where B_2 and B_3 are temperature and stress dependent constants. The above relations are applicable when more than one mechanism deformation contributes to the damage accumulation in the tertiary stage.

Figure 7(a) shows the creep strains e_2 and e_3 with time on a linear scale at 1145 K. Figure 7(b) shows the same strains as described by the above equations in the second and third stages on the log-log plot. Figure 8 shows the relation between creep strain and time at 1255 K on the log-log plot. The exponent

[X3] is the slope of tertiary strain versus time on that log-log plot. The values of X3 for the four temperatures used in this study have been found to be 2, 3, 4.5 and 5.2, respectively.

Near the end of the tertiary stage, the strain is localized due to necking and the strain rate in this region becomes very high. Thus, in many cases, the data points near rupture will deviate from linearity on the log-log plot, as can be seen in the Fig. 8. At 1035 K, primary creep was observed at all stress levels, and this first stage creep strain has been subtracted from the total strain to obtain the secondary and tertiary creep strains.

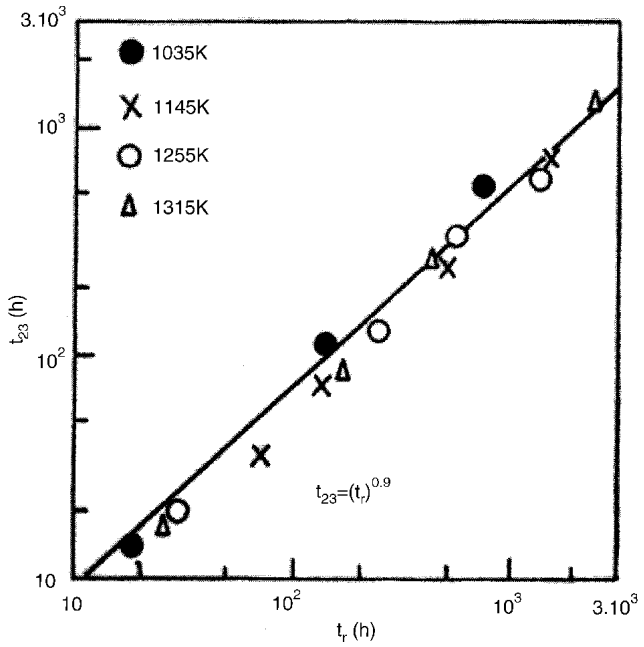

Fig. 6 Relation between t_{23} and t_r

From geometric considerations[10,11] it can be shown that

$$\dot{e}_s\, t_r = (e_{23}^{(X3-1)}\, e_r)^{\frac{1}{X3}} = C_R \qquad \text{(Eq 5)}$$

when X3 = 1, the above equation leads to the modified Monkman-Grant relation. When X3 = 2, the relation becomes

$$\dot{e}_s\, t_r = \sqrt{(e_{23}\, e_r)} \qquad \text{(Eq 6)}$$

as noted by Phaniraj et al.[12] However, if e_{23} and/or e_r depend on the rupture time t_r, then the above equation can be generalized as

$$\dot{e}_s\, t^a = \text{constant} \qquad \text{(Eq 7)}$$

where a is a constant.[12]

In the present investigation, the exponent X3 varies from 2 to 5.2 as the temperature increases. Measuring the values of e_{23} and e_r, C_R has been computed and the relation between $\dot{e}_s/(e_{23}^{(X3-1)}\, e_r)^{1/X3}$ and t_r determined. This is shown in Fig. 9 on a log-log plot. The agreement appears to be very good and the scatter observed in Fig. 4 has been reduced to a minimum. The slope of the line is equal to unity and $[\dot{e}_s t_r/C_R]$ is equal to one. Determination of the strain values e_{23} and e_r will not present much of a problem if the data are plotted on the log-log scale.

3.2 Microstructural Analysis

Figure 10(a-c) show the SEM micrographs of studies conducted on specimens crept at 1035 K. Though coarsening of the γ′ particles is noticed, it is not pronounced and the cuboidal shape has remained unaltered as can be seen in Fig. 10(a). Decohesion between the matrix and the carbide particles have

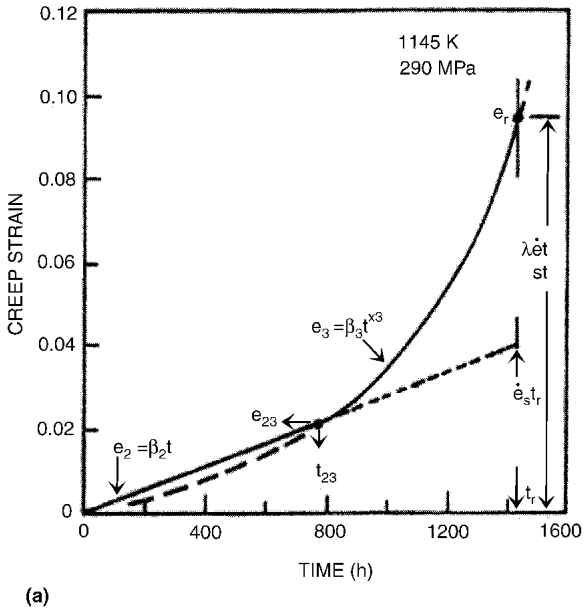

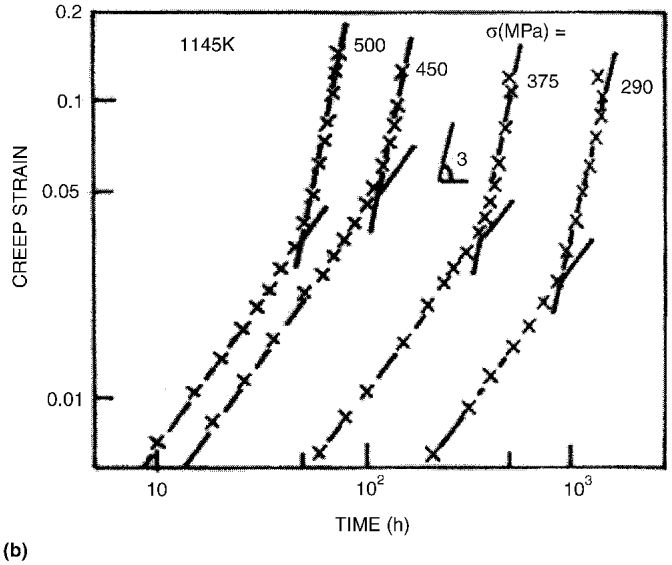

Fig. 7 Representation of secondary and tertiary creep strain with time on **(a)** normal scale and **(b)** log-log scale

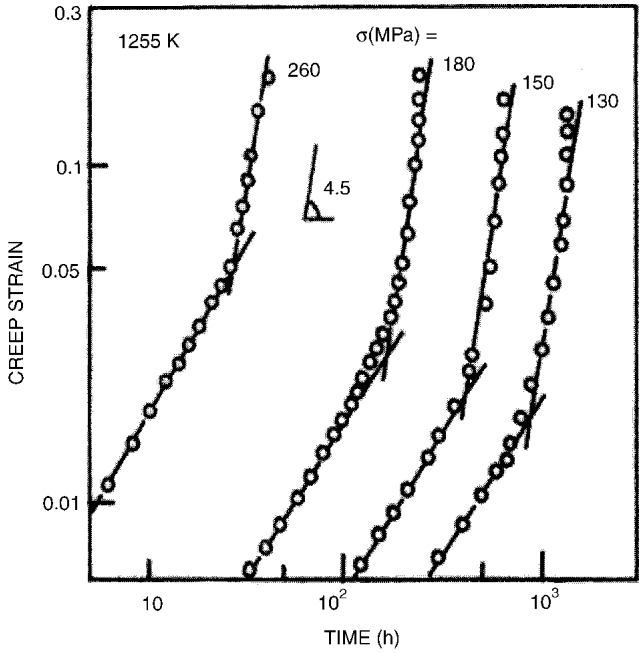

Fig. 8 Relation between secondary and tertiary creep strains with time at 1255 K on a log-log plot

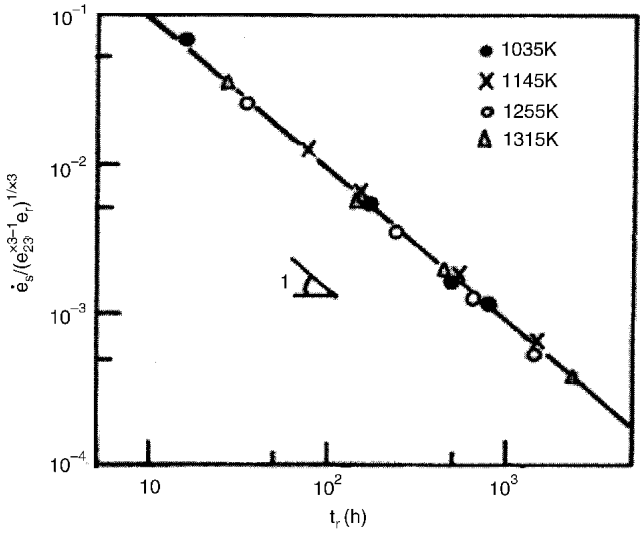

Fig. 9 Relation between the modified $\dot{e}_s$ and t_r

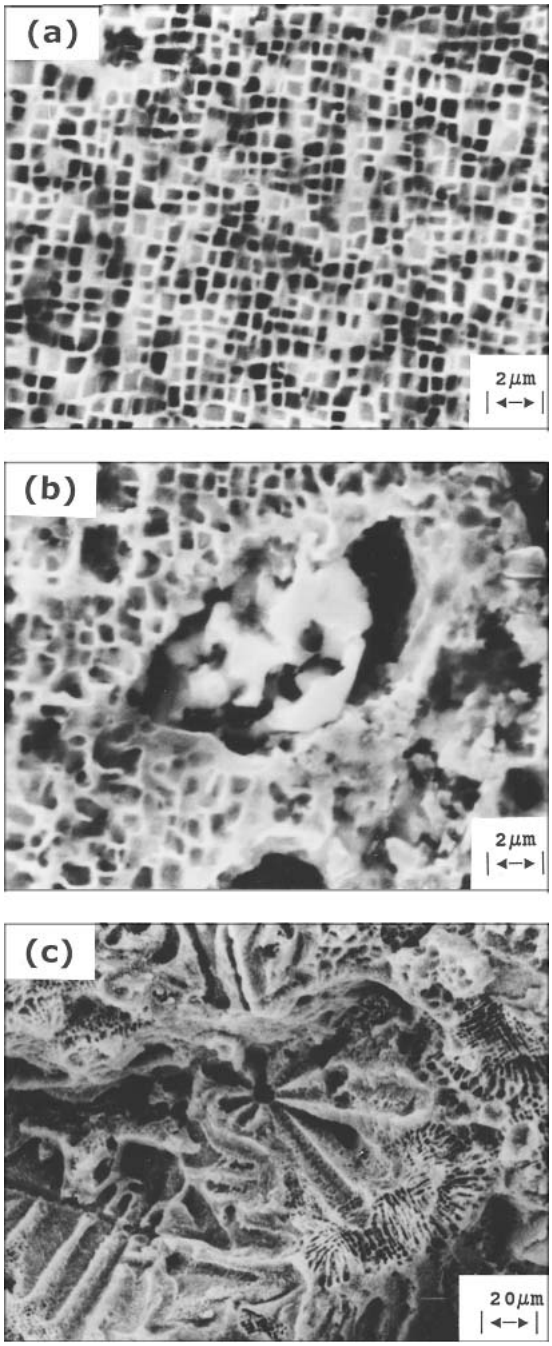

Fig. 10 SEM micrographs of specimens crept at 1035 K. Cuboidal shape of γ′ remains almost unaltered; decohesion between matrix and carbide particle, and faceted fracture observed

been observed (Fig. 10b). The alloy showed faceted fracture with crack like voids nucleating around carbide particles and in the γ-γ′ eutectic regions (Fig. 10c). In the TEM micrographs of the fractured specimens, dislocations within the γ′ particles have been observed, i.e., particle cutting is seen in the final stages of fracture.[6] The fracture is mixed mode for small tertiary creep strain, i.e., it varied in the range of 0.01-0.016. It may also be noted in Fig. 2 that at this temperature the tensile strength level is high and the ductility is comparatively low.

Figure 11(a-e) show SEM micrographs of fracture surfaces of specimens crept at 1145 K. At this temperature thermally activated slip systems become more active. Though not pronounced, coarsening of γ′, and their coalescence, can be noticed (Fig. 11a). Specimens exposed to high temperature for a longer duration (low-stress creep) showed decohesion of the matrix from the carbide particles and also increased coarsening (Fig. 11b and c). Uniform creep cavitation within the DS grains is also observed. There are no grain boundary voids or cracks. The fracture surfaces revealed plastic deformation as evidenced by void growth, though some small areas of faceted fracture

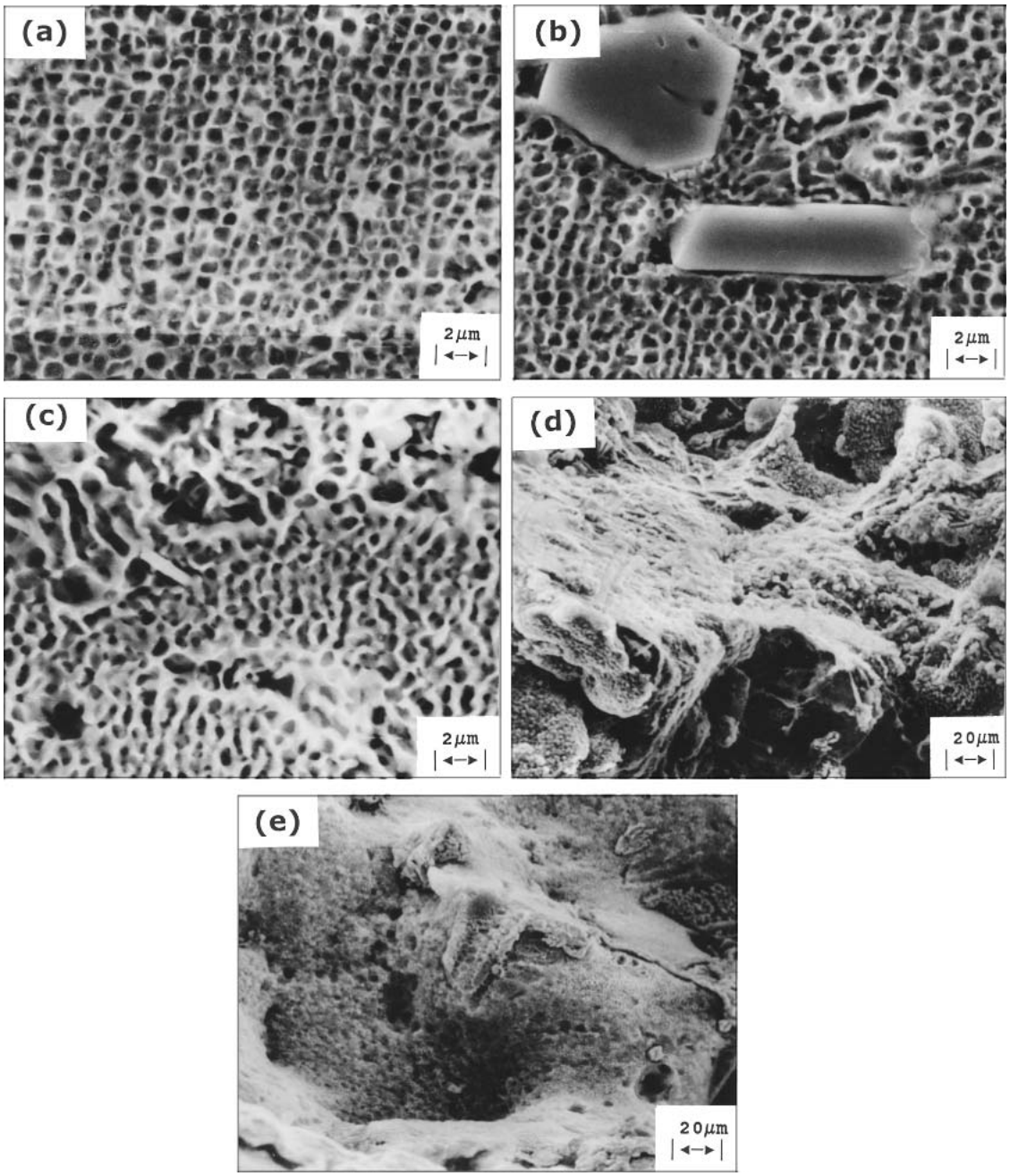

Fig. 11 SEM micrographs of specimens crept at 1145 K: **(a)** coarsening of γ′ particles and their coalescence: **(b,c)** decohesion of matrix and increased coarsening with longer exposure, **(d,e)** void formation and ductile fracture

were also observed (Fig. 11e). The tertiary creep strain increases at this temperature and the creep ductility index (λ) varies from 2 to 4.

Figure 12(a-c) show the micrographs of specimens crept at 1255 K. At this temperature and for this length of time, the coarsening, of γ′ is almost complete. Coalescence of these coarsened particles leads to the formation of "rafts" perpendicular to the loading direction. Voids can be observed along the γ-γ′ interface (Fig. 12a and b). Decohesion takes place around the carbide particles. Figure 12(d-e) show SEM of fractured surfaces that indicate a ductile transgranular mode of failure. The failure has occurred due to the crack-like cavity growth along the γ-γ′ interface in the direction normal to the applied load.

The fracture mode at 1315 K is, more or less, similar to that at 1255 K with the alloy showing a large tertiary creep regime. Large-scale rafting of γ′ is noticed. Void nucleation and tearing of the γ-γ′ interface are also observed. The most striking feature is the crack-like growth of the voids and decohesion around the carbide particles. During the initial stages of creep deformation, well-defined γ′ rafts develop in the alloy, and the γ-γ′ mismatch strain aids in their growth. This process occurs

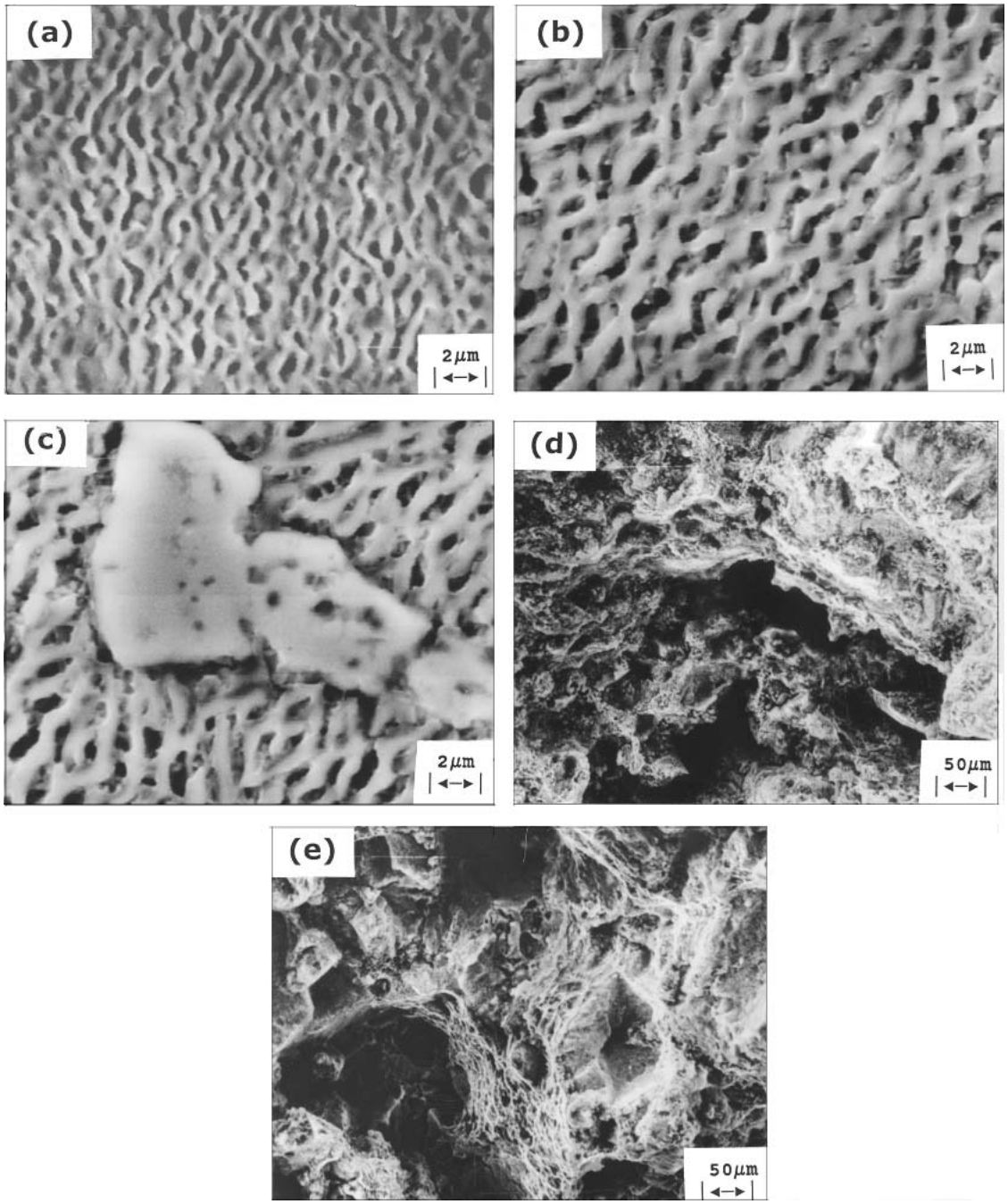

Fig. 12 SEM micrograph of specimens crept at 1255 K: **(a,b)** voids along the γ-γ′ interface, **(c)** decohesion along the raft, and **(d,e)** cavity growth and ductile fracture

normal to the direction of the applied stress. Such type of raft formation and void growth has been reported in the literature.[13,14] The creep ductility index (λ) lies in the range of 5-10 with a creep rupture strain between 15% and 20%.

Figure 13 shows the stress-rupture time relation of the alloy at the four test temperatures. Three important failure mode zones can be identified. At 1035-1100 K, faceted fracture is expected with cracking possibly nucleating from the decohesion zones. Upon increasing the temperature to 1145 K, thermally activated mechanisms control deformation, and creep ductility increases. Coarsening of γ′ takes place along with void formation in the decohesion zones. At higher temperatures coarsening of γ′ and their coalescence and rafting are observed. There is decohesion between the γ′ particles and the γ matrix in the raft region, and crack-like voids grow which lead to specimen failure. Due to increased microstructure instability and dislocation motion, the creep ductility index (λ) increases at these temperatures.

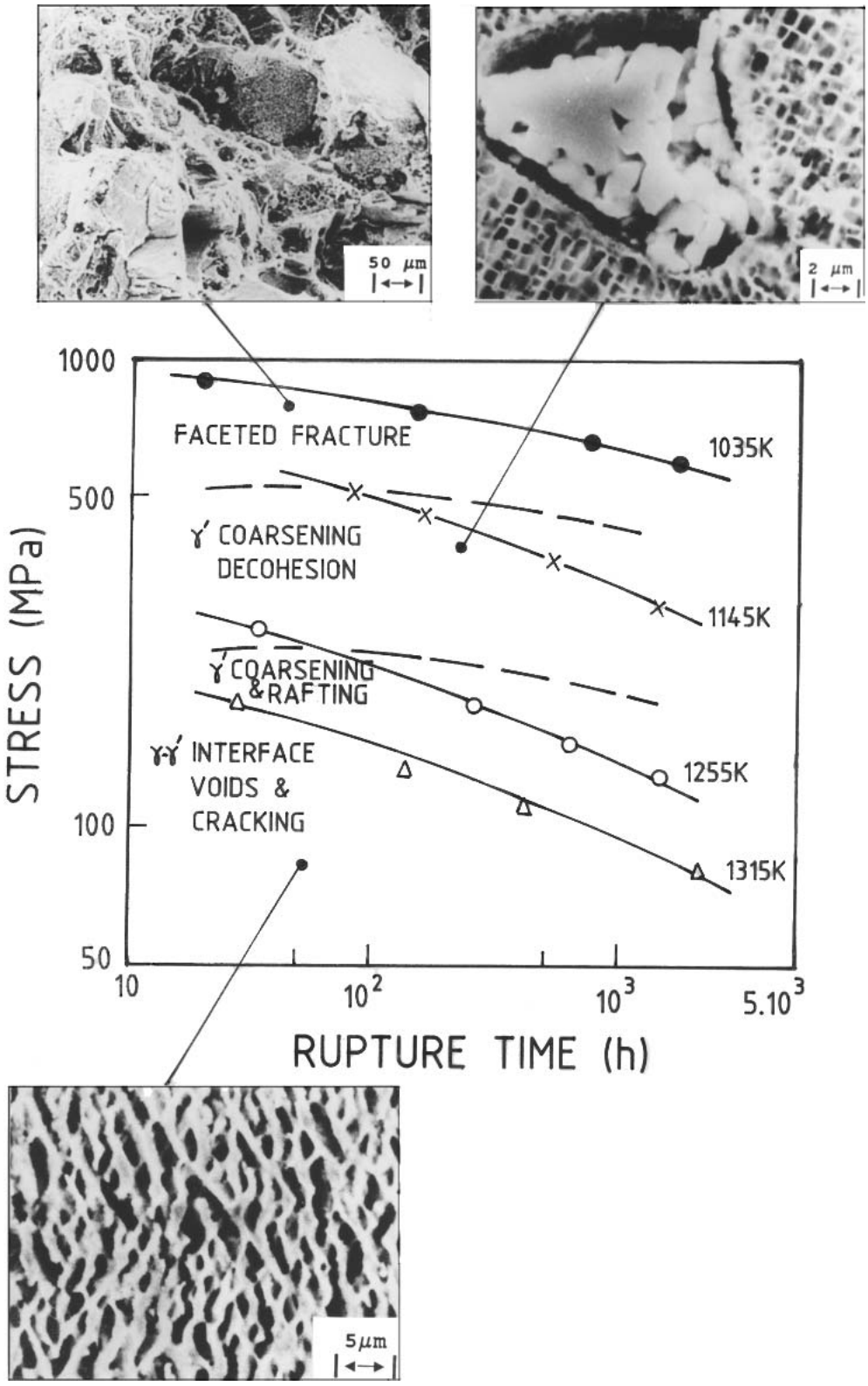

Fig. 13 Creep stress-rupture time relation

3.3 Creep Ductility and Failure Diagnostic Diagram

At 1035 K fracture is faceted with some cavities. Creep ductility is low. The ductility index (λ) is close to 1.4. At higher temperatures coarsening of γ′ dominates with decohesion at carbide precipitates and crack-like void formation at the γ-γ′ interface. The creep ductility index (λ) also increases. Considering the tertiary creep stage at 290 MPa and 1145 K, it was found that the creep rate near end of the tertiary stage (leaving out the fast fracture zone due to necking at the end) is around 10-15 times the minimum creep rate ($\dot{e}_s$). The tertiary creep strain (e_3) can be expressed as

$$e_3 = B_3\, t^{X3} = B_{30}\,(\dot{e}_s\, t) t^{(X3-1)} \qquad \text{(Eq 8a)}$$

or,

$$\frac{e_3}{\dot{e}_s\, t} = B_{30}\, F_o\,(t) \qquad \text{(Eq 8b)}$$

where B_{30} is a constant and $F_o(t)$ is a function of time. This function of time is determined by the mechanisms that act during the tertiary creep stage. Considering γ′ coarsening, the tertiary creep rate ($\dot{e}_3$) can be written as[15,16]

$$\frac{\dot{e}_3}{\dot{e}_s} = \left[\frac{1 - \dfrac{\sigma_o}{\sigma(1+pt)}}{1 - \dfrac{\sigma_o}{\sigma}} \right]^{1/3} \qquad \text{(Eq 9)}$$

where σ_o is the initial back stress (= $a\,G\,b/l_o$); G is the shear modulus; B is the Burgers vector; l_o is the initial particle spacing; σ is the applied stress; p is the kinetic rate constant; and n is the creep stress exponent.

Figure 14 shows the increase in tertiary creep strain rate with time at 1145 K and 300 MPa due to γ′ coarsening. Typical values of the constants used in Eq 9 are indicated in the figure. For a tertiary time of around 500 h, the creep rate has increased 5-10 times that of the minimum value. Other mechanisms may also contribute to the deformation process and the tertiary creep rate.

Ashby and Dyson[17] have proposed a diagnostic diagram for creep failure based on λ. A form of the diagram is shown in Fig. 15, which illustrates the relation between creep strain and λ on a log-log plot. Creep ductility index and time fraction (t_r/t_{23} = *1/f*) lines are also shown in the figure. The creep ductility index and *1/f* are related through the following expression:

$$\lambda = \left(\frac{1}{f}\right)^{(X3-1)} \qquad \text{(Eq 10)}$$

If X3 = *2* (i.e., parabolic law for the tertiary creep strain), then λ = *1/f*. As a typical example, the creep strain for the material at 1145 K and 290 MPa is shown in Fig. 15. When the quantity ($\dot{e}_s\, t$) is equal to e_{23}, the secondary creep stage terminates and the tertiary one starts. The slope of the line is determined by the value of X3. The governing mechanisms of deformation and the different modes of failure at different levels

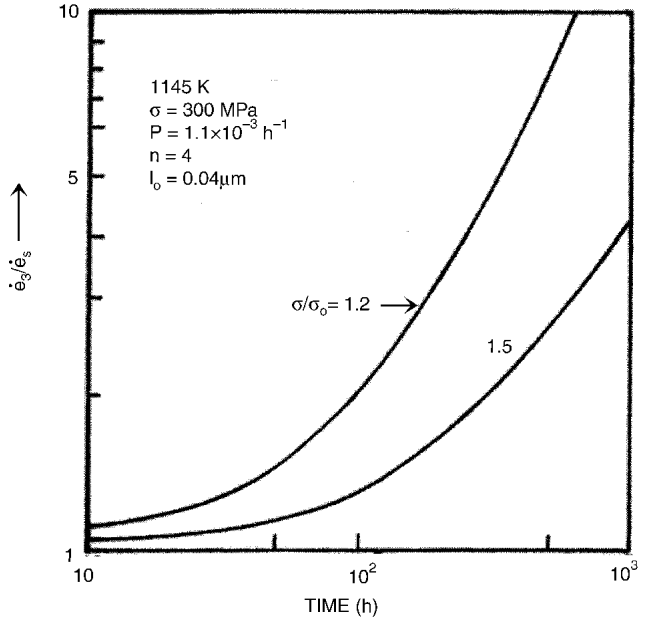

Fig. 14 Increase in tertiary creep strain rate, $\dot{e}_3$, with time due to γ′ coarsening

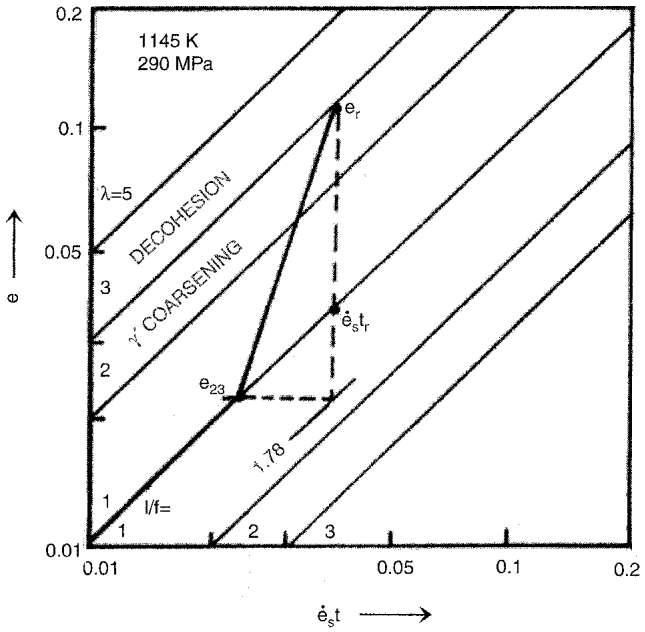

Fig. 15 Typical creep failure diagnostic diagram at 1145 K

of λ are also illustrated in this figure. For λ up to 1.5, faceted or brittle failure can be expected. When λ lies in the range of 2-3, extensive microstructural changes followed by void formation may be the dominant features. Beyond this range, large scale coarsening and rafting, with subsequent crack-like voids forming, are possible.

Figure 16 and 17 illustrate the creep failure diagnostic diagrams at temperatures of 1035 and 1255 K, respectively, for the stress ranges used in the investigation. At 1035 K, creep duc-

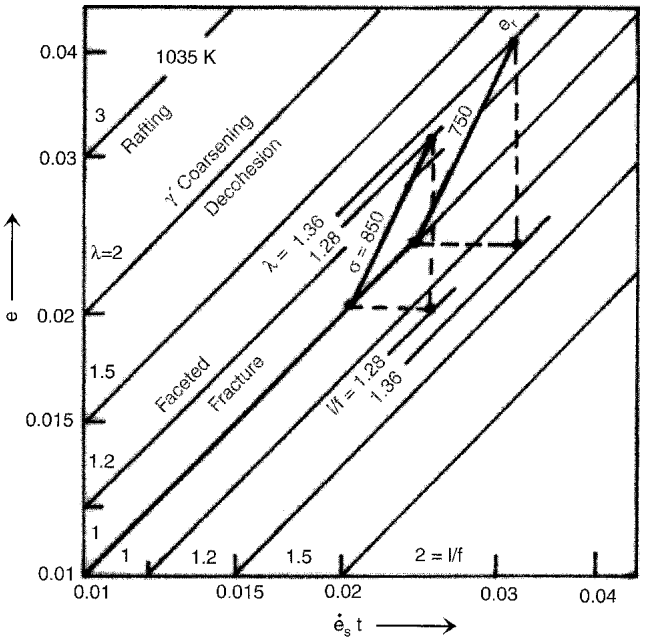

Fig. 16 Creep failure diagnostic diagram at 1035 K

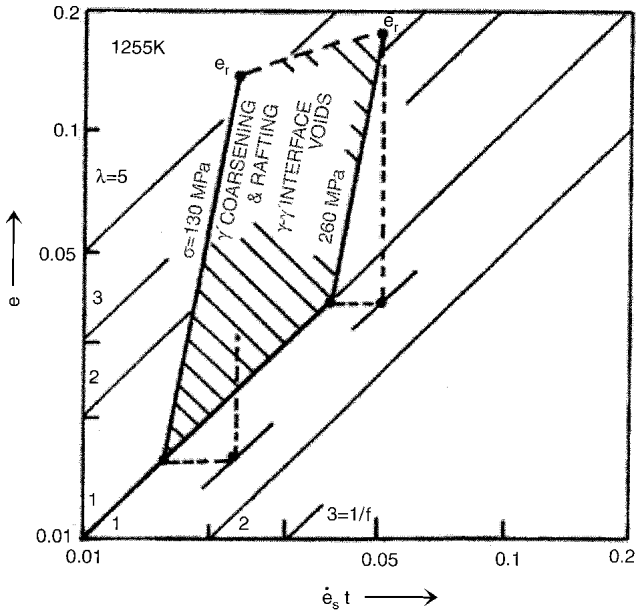

Fig. 17 Creep failure diagnostic diagram at 1255 K

tility is small while it is large at 1255 K, and the applicable λ regimes are shown on these diagnostic diagrams.

4. Conclusions

From the experimental and mathematical analysis carried out on a DS cast Ni-base superalloy, the following observations and conclusions have been noted:

- Optical and TEM studies revealed for the alloys tested, the microstructure consists of fine carbides, a dendritic substructure within columnar grains and cuboidal γ′ particles. The γ′ particles are 0.4 μm in size with an inter-particle spacing of ~0.04 μm.
- Creep experiments carried out at 1035 K indicated primary creep followed by the secondary and tertiary stages. However, the tertiary creep regimen is not very pronounced and the creep ductility index (λ) is low at this temperature.
- Creep experiments carried out at 1145 K, and above, indicated only secondary and tertiary creep stages. The tertiary creep stage became more pronounced as the temperature increased, and λ also increased with increasing temperature.
- The secondary and tertiary creep regimes can be described by simple power functions of time: $e_2 = B_2 t$ and $e_3 = B_3 t^{X3}$, where X3 depends on the temperature.
- The Monkman-Grant relation can be given by: $\dot{e}_s t_r = (e_{23}{}^{X3-1}\ e_r)^{1/X3}$, where e_{23} is the creep strain at the end of the secondary stage.
- The duration of the secondary stage (t_{23}) appears to be a simple power law relation with the rupture time (t_r): $t_{23} = C\ t_r^{0.9}$, where C = 1.
- Creep fracture at 1035 K is faceted in nature with very small voids. The γ′ particles maintain their shape and there is not much coarsening. At 1145 K the γ′ particles coarsen with decohesion at the carbide particles occurring. Ductile voids are seen on the fractured surfaces. At still higher temperatures, γ′ coarsening is significant with the formation of rafts. There is decohesion between the matrix and the raft. Void formation and subsequent decohesion enhance the tertiary creep deformation mechanisms at higher temperatures.
- Based on the observations of the creep deformation and the governing deformation relations, the creep failure diagnosis diagram proposed by Ashby and Dyson has been developed and presented for the alloy investigated.

Acknowledgments

The authors gratefully acknowledge the financial support received from the Defense Research Development Organization (DRDO), New Delhi, India for carrying out this research work. The work presented here formed a part of PhD dissertation submitted to Indian Institute of Technology (IIT), Madras, India by the first author.

References

1. J.J. Jackson, M.J. Donachie, R.J. Henricks, and M. Gell: *Metall. Trans. A,* 1977, *8A,* p. 1615-20.
2. M. McLean: *Directionally Solidified Materials for High Temperature Service,* The Metals Society, London, UK, 1983.
3. P.N. Quested and S. Osgerby: *Mater. Sci. Technol.,* 1986, *2,* p. 461.
4. B. DeMestral, G. Eggeler, and H.J. Klan: *Metall. Materials Trans.,* 1996, *27A,* p. 879.
5. M. Gell and D.N. Duhl: *Processing and Properties of Aadvanced High Temperature Alloys,* S. Allen et.al, ed., ASM, Metals Park, OH, 1986, p. 41.
6. M.S. Gopalakrishna, A.M. Sriramamurthy, and V.M. Radhakrishnan: *Scripta Mater.,* 1996, *35*(11), p. 1325.
7. M.S. Gopalakrishna: "Studies on Creep and Creep Crack Growth Be-

havior of a DS Cast Ni-Base Alloy," Ph.D. Thesis, Indian Institute of Technology, Madras, India, 1997.

8. R.W. Evans and B. Wilshire: *Creep of Metals and Alloys,* The Institute of Metals, London, UK, 1985.
9. V.M. Radhakrishnan: *J. Mater. Eng. Perf.,* 1992, *1,* p. 123.
10. V.M. Radhakrishnan, P.J. Ennis, and H. Schuster: "An Analysis of Creep Deformation and Rupture by the β-Envelope Method," KFA-Julich Report, No. 2535, Julich, Germany, Oct 1991.
11. M.S. Gopala Krishna, A.M. Sriramamurthy, and V.M. Radhakrishnan: *J. Mater. Eng. Perf.,* 1998, *7*(4), p. 548.
12. C. Phaniraj, M. Nandagopal, S.L. Mannan, P. Rodrigurz, and B.P. Kashyap: *Acta. Mater.,* 1996, *44*(10), p. 4059.
13. V.M. Radhakrishnan: *Fatigue Fract Eng. Mater Struct.,* 1992, *3,* p. 617.
14. S.J. Moss, G.A. Webster, and E. Fluery: *Metall Mater Trans. A,* 1996, *15*(6), p. 829.
15. J. Gue, D. Ranucci, E. Picco, and P.M. Stroncchi: *Metall Trans. A,* 1983, *14A,* p. 2329.
16. G. Sundarrajan: *Trans Ind. Inst. Metals,* 1989, *42,* p. s189.
17. M.F. Ashby and B.F. Dyson: in *Proc. 6th Inter Conf. on Fracture,* Pergamon Press, Oxford, UK, 1984, p. 1.